Available online at www.sciencedirect.com
SCIENCE DIRECT®
Computers & Fluids 35 (2006) 326–348
computers & fluids
www.elsevier.com/locate/compfluid

The 2D lid-driven cavity problem revisited

Charles-Henri Bruneau *, Mazen Saad

Mathématiques Appliquées de Bordeaux, Université Bordeaux 1, 351 cours de la Libération, 33405 Talence, France

Received 16 September 2003; received in revised form 15 June 2004; accepted 1 December 2004
Available online 19 April 2005

Abstract

Numerical simulations of the 2D lid-driven cavity flow are performed for a wide range of Reynolds numbers. Accurate benchmark results are provided for steady solutions as well as for periodic solutions around the critical Reynolds number. Numerous comparisons with the results available in the literature are given. The first Hopf bifurcation is localized by a study of the linearized problem.

PACS: 65D99; 65P40; 76D05; 76D17; 76F65

1. Introduction

The classical lid-driven cavity problem has been investigated by many authors since some pioneer works giving good results of steady solutions twenty years ago [8,20]. Their results were confirmed by many other studies and the solution obtained at $Re = 1000$ for instance is quite close from one author to another. Nevertheless there still are very different results concerning the first Hopf bifurcation and the behaviour of the solution for intermediate and high Reynolds numbers. In a former work [5], it was suggested that the first Hopf bifurcation occurs around Reynolds number $Re = 7500$. Since then various results were given in the literature. This first bifurcation

* Corresponding author.
E-mail addresses: bruneau@math.u-bordeaux.fr (C.-H. Bruneau), saad@math.u-bordeaux.fr (M. Saad).

0045-7930/$ - see front matter
doi:10.1016/j.compfluid.2004.12.004

was given under $Re = 7500$ in [6] or [18], close to $Re = 8000$ in [7], [2] or [19] while some authors localize it at $Re = 10{,}000$ and even close to $Re = 30{,}000$ [12]. The aim of this work is to shed some light on this fundamental issue and to give benchmark results for Reynolds numbers up to $Re = 10{,}000$.

The numerical simulation lie on a finite differences discretization and on a multigrid solver with a cell-by-cell relaxation procedure [22,5]. Classical Euler or Gear time schemes are coupled to a second-order approximation of the linear terms in space. To achieve a good accuracy a special care of convective terms is required. In this work, they are treated explicitly and approximated by third-order schemes to get both low diffusion effects and stability. A new third-order scheme is constructed and compared to the classical ones, namely the original third-order upwind scheme, the quickest scheme [16] and an other upwind scheme based on a centered stencil [13].

The next section is devoted to the governing equations and the time and space discretization. Then the multigrid solver is described and a special emphasis is given on the discretization of convection terms. We recall three third-order schemes and construct carefully a fourth one which is compared to the others on accurate benchmark results for steady solutions at $Re = 1000$ and $Re = 5000$. Then, by computing the first Lyapunov exponent, we study the linear stability to determine the critical Reynolds number Re_c corresponding to the first Hopf bifurcation. This study shows that this critical Reynolds number Re_c is close to $Re = 8000$. Further, we compute some periodic solutions beyond this value and in particular the solution at $Re = 10{,}000$. For all these results until $Re = 10{,}000$, the grid convergence is achieved and reliable results are obtained on an uniform 512×512 cells grid.

2. Governing equations and discretization

2.1. The Navier–Stokes equations

Let $\Omega = (0,1) \times (0,1)$ be a 2D square cavity and $T > 0$ the simulation time, the governing equations of an unsteady incompressible flow are the evolution Navier–Stokes equations written in primitive variables as:

$$\begin{cases} \partial_t U - \dfrac{1}{Re}\Delta U + (U \cdot \nabla)U + \nabla p = 0 & \text{in }]0,T[\times \Omega \\ \nabla \cdot U = 0 & \text{in }]0,T[\times \Omega \\ U(t,x,y) = (-1,0) & \text{on }]0,T[\times \Gamma_1 \\ U(t,x,y) = (0,0) & \text{on }]0,T[\times \Gamma_0 \\ U(0,x,y) = U_0(x,y) & \text{in } \Omega \end{cases} \tag{1}$$

where $U = (u,v)$ and p are, respectively, the velocity and the pressure, Γ_1 is the top boundary, Γ_0 represents the three other sides and U_0 is an initial datum. The boundary condition is chosen so that the primary vortex is positive. Most of the time, the flow is assumed to start from rest and thus $U_0 = 0$.

2.2. Time discretization

The system of equation (1) is discretized by means of either a first-order Euler scheme or a second-order Gear scheme. The linear terms are treated implicitly whereas the convection terms are treated explicitly. We denote by U^n the approximation of U at time $t_n = n\delta t$ where $n \in \mathbb{N}$ and δt is the time step. Thus, the Euler semi-discretized system reads

$$\begin{cases} \dfrac{U^n}{\delta t} - \dfrac{1}{Re}\Delta U^n + \nabla p^n = \dfrac{U^{n-1}}{\delta t} - (U^{n-1}\cdot\nabla)U^{n-1} & \text{in } \Omega \\ \nabla \cdot U^n = 0 & \text{in } \Omega \\ U^n = (-1,0) & \text{on } \Gamma_1 \\ U^n = (0,0) & \text{on } \Gamma_0 \end{cases} \tag{2}$$

and the Gear semi-discretized system reads

$$\begin{cases} \dfrac{3U^n}{2\delta t} - \dfrac{1}{Re}\Delta U^n + \nabla p^n = \dfrac{2U^{n-1}}{\delta t} - 2(U^{n-1}\cdot\nabla)U^{n-1} - \dfrac{U^{n-2}}{2\delta t} + (U^{n-2}\cdot\nabla)U^{n-2} & \text{in } \Omega \\ \nabla \cdot U^n = 0 & \text{in } \Omega \\ U^n = (-1,0) & \text{on } \Gamma_1 \\ U^n = (0,0) & \text{on } \Gamma_0 \end{cases} \tag{3}$$

We shall see in the last sections the difference between these two schemes. Of course to compute steady solutions the influence of the time scheme is weak but for evolution solutions it can be of main importance.

2.3. Space discretization

The system of equations (2) or (3) is discretized in space by finite differences on an uniform staggered grid G_h the mesh size of which is $h = \delta x = \delta y$, where δx and δy are the step discretization in each direction. The discrete values of the pressure are located at the center of each cell and those of the velocity field are located at the middle of the sides as shown in Fig. 1.

The discretization of the left-hand side of equations (2) or (3) or is achieved using second-order centered finite differences. For a generic inner cell that means that for instance

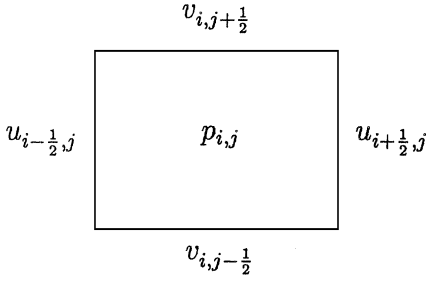

Fig. 1. A staggered cell.

$$\frac{u^n}{\delta t} - \frac{1}{Re}\Delta u^n + \partial_x p^n$$

is approximated at point $(i-\frac{1}{2}, j)$ by

$$\frac{u^n_{i-\frac{1}{2},j}}{\delta t} - \frac{1}{Re}\left(\frac{u^n_{i+\frac{1}{2},j} - 2u^n_{i-\frac{1}{2},j} + u^n_{i-\frac{3}{2},j}}{\delta x^2} + \frac{u^n_{i-\frac{1}{2},j+1} - 2u^n_{i-\frac{1}{2},j} + u^n_{i-\frac{1}{2},j-1}}{\delta y^2}\right) + \frac{p^n_{i,j} - p^n_{i-1,j}}{\delta x}$$

Let us point out to the reader that due to the use of staggered grids the discretization of the diffusion terms at the boundary with a second-order schemes yields modified formulas as

$$(\partial_{yy}u)_{i-\frac{1}{2},1} \approx \left(\frac{8}{3}u_{i-\frac{1}{2},\frac{1}{2}} - 4u_{i-\frac{1}{2},1} + \frac{4}{3}u_{i-\frac{1}{2},2}\right)\Big/(\delta y)^2 \text{ with } u_{i-\frac{1}{2},\frac{1}{2}} = 0 \text{ on the bottom wall}$$

The second equation of the momentum equation for the component v is discretized in the same way. The divergence-free equation is approximated at the pressure point (i,j) by

$$\frac{u^n_{i+\frac{1}{2},j} - u^n_{i-\frac{1}{2},j}}{\delta x} + \frac{v^n_{i,j+\frac{1}{2}} - v^n_{i,j-\frac{1}{2}}}{\delta y} = 0.$$

This point is crucial as it links the four velocity components of the same cell. The convection terms in the right-hand side of equations (2) are approximated by the third-order Murman-like scheme constructed in Section 4. For instance

$$\frac{u^{n-1}}{\delta t} - u^{n-1}\partial_x u^{n-1} - v^{n-1}\partial_y u^{n-1}$$

is approximated at point $(i-\frac{1}{2}, j)$ by

$$\frac{u^{n-1}_{i-\frac{1}{2},j}}{\delta t}$$

$$-\frac{u^{n-1}_{i,j}}{3}\frac{\Delta_{i,j}u^{n-1}}{\delta x} - \frac{5u^{n-1}_{i-1,j}}{6}\frac{\Delta_{i-1,j}u^{n-1}}{\delta x} + \frac{u^{n-1}_{i-2,j}}{6}\frac{\Delta_{i-2,j}u^{n-1}}{\delta x} \quad \text{if } u^{n-1}_{i-1,j} > 0$$

$$-\frac{u^{n-1}_{i-1,j}}{3}\frac{\Delta_{i-1,j}u^{n-1}}{\delta x} - \frac{5u^{n-1}_{i,j}}{6}\frac{\Delta_{i,j}u^{n-1}}{\delta x} + \frac{u^{n-1}_{i+1,j}}{6}\frac{\Delta_{i+1,j}u^{n-1}}{\delta x} \quad \text{if } u^{n-1}_{i,j} < 0$$

$$-\frac{v^{n-1}_{i-\frac{1}{2},j+\frac{1}{2}}}{3}\frac{\Delta_{i-\frac{1}{2},j+\frac{1}{2}}u^{n-1}}{\delta y} - \frac{5v^{n-1}_{i-\frac{1}{2},j-\frac{1}{2}}}{6}\frac{\Delta_{i-\frac{1}{2},j-\frac{1}{2}}u^{n-1}}{\delta y} + \frac{v^{n-1}_{i-\frac{1}{2},j-\frac{3}{2}}}{6}\frac{\Delta_{i-\frac{3}{2},j-\frac{3}{2}}u^{n-1}}{\delta y} \quad \text{if } v^{n-1}_{i-\frac{1}{2},j-\frac{1}{2}} > 0$$

$$-\frac{v^{n-1}_{i-\frac{1}{2},j-\frac{1}{2}}}{3}\frac{\Delta_{i-\frac{1}{2},j-\frac{1}{2}}u^{n-1}}{\delta y} - \frac{5v^{n-1}_{i-\frac{1}{2},j+\frac{1}{2}}}{6}\frac{\Delta_{i-\frac{1}{2},j+\frac{1}{2}}u^{n-1}}{\delta y} + \frac{v^{n-1}_{i-\frac{1}{2},j+\frac{3}{2}}}{6}\frac{\Delta_{i-\frac{3}{2},j+\frac{3}{2}}u^{n-1}}{\delta y} \quad \text{if } v^{n-1}_{i-\frac{1}{2},j+\frac{1}{2}} < 0$$

where $u^{n-1}_{i,j} = \frac{1}{2}\left(u^{n-1}_{i+\frac{1}{2},j} + u^{n-1}_{i-\frac{1}{2},j}\right)$ and $v^{n-1}_{i-\frac{1}{2},j+\frac{1}{2}} = \frac{1}{2}\left(v^{n-1}_{i,j+\frac{1}{2}} + v^{n-1}_{i-1,j+\frac{1}{2}}\right)$ are obtained by linear interpolation, $\Delta_{i,j}u^{n-1} = \left(u^{n-1}_{i+\frac{1}{2},j} - u^{n-1}_{i-\frac{1}{2},j}\right)$ and $\Delta_{i-\frac{1}{2},j+\frac{1}{2}}u^{n-1} = \left(u^{n-1}_{i-\frac{1}{2},j+1} - u^{n-1}_{i-\frac{1}{2},j}\right)$.

The corresponding term for the vertical component of the velocity v is discretized in the same way. The construction of this scheme is presented in Section 4 where we give a comparison of various third-order schemes.

3. Multigrid solver

The discretization of the coupled velocity–pressure system of equations (2) or (3) yields to solve a discrete linear system $L_h V_h^n = B_h^{n-1}$ or $L_h V_h^n = C_{1,h}^{n-1} + C_{2,h}^{n-1}$ where L_h represents the discrete operator, B_h^{n-1} is the discrete equivalent of the right-hand side of (2), $C_{1,h}^{n-1} + C_{2,h}^{n-1}$ is the discrete equivalent of the right-hand side of (3) and $V_h^n = (U_h^n, p_h^n)$ is the approximate solution to compute. We solve this discrete linear system by the FAS multigrid solver [11] on a sequence of grids from the fine grid chosen for the approximation G_p to a coarsest grid G_1 as coarse as 4×4 cells. The multigrid algorithm uses a V-cycle procedure illustrated below for the computation of the fine grid solution $V_h^n = V_p^n$ on grid G_p in the case of system (2).

$$
\left\{
\begin{array}{l}
\text{For } k = 1 \text{ to number\_of\_V-cycles do} \\
\widetilde{V}_p^k = S_p^{(\nu_1)}(L_p, V_p^{k-1}, B_p^{n-1}) \\
\text{Correction on coarse grids} \\
\left\{
\begin{array}{l}
\text{For } q = p-1, 1, -1 \text{ do} \\
\overline{V}_q^k = R_q^{q+1} \widetilde{V}_{q+1}^k \\
B_q^k = R_q^{q+1}\left(B_{q+1}^k - L_{q+1}\widetilde{V}_{q+1}^k\right) + L_q \overline{V}_q^k \\
\widetilde{V}_q^k = S_q^{(\nu_1)}(L_q, \overline{V}_q^k, B_q^k)
\end{array}
\right. \\
\text{Updating of the fine grids} \\
\left\{
\begin{array}{l}
\text{For } q = 2, p \text{ do} \\
\widehat{V}_q^k = \widetilde{V}_q^k + P_{q-1}^q\left(V_{q-1}^k - \overline{V}_{q-1}^k\right) \\
V_q^k = S_q^{(\nu_2)}\left(L_q, \widehat{V}_q^k, B_q^k\right)
\end{array}
\right. \\
\text{Convergence test} \\
\text{if } \|B_p^{n-1} - L_p V_p^k\| \leqslant \epsilon \text{ stop iterations}
\end{array}
\right.
$$

In this algorithm $S_q^{(\nu)}$ denotes the smoother used on grid G_q to compute an approximate solution of the linear system doing ν iterations. The restriction R_q^{q+1} and prolongation P_{q-1}^q operators describe the linear interpolation operators from fine-to-coarse and from coarse-to-fine grids respectively. Moreover, the second member that contains the convective term is discretized only on the finest grid G_p and the second member on the coarse grids B_q^k is mainly obtained by restriction.

The smoothing operator S performs ν_1 or ν_2 iterations of a Gauss–Seidel cell-by-cell procedure that leads to solve a 5×5 linear system corresponding to the five unknowns of a cell [22].

$$
\begin{pmatrix}
\alpha & 0 & 0 & 0 & 1/\delta x \\
0 & \alpha & 0 & 0 & -1/\delta x \\
0 & 0 & \alpha & 0 & 1/\delta y \\
0 & 0 & 0 & \alpha & -1/\delta y \\
-1/\delta x & 1/\delta x & -1/\delta y & 1/\delta y & 0
\end{pmatrix}
\begin{pmatrix}
u^n_{i-\frac{1}{2},j} \\
u^n_{i+\frac{1}{2},j} \\
v^n_{i,j-\frac{1}{2}} \\
v^n_{i,j+\frac{1}{2}} \\
p^n_{i,j}
\end{pmatrix}
=
\begin{pmatrix}
(D_h^{n-1})_{i-\frac{1}{2},j} \\
(D_h^{n-1})_{i+\frac{1}{2},j} \\
(D_h^{n-1})_{i,j-\frac{1}{2}} \\
(D_h^{n-1})_{i,j+\frac{1}{2}} \\
0
\end{pmatrix}
$$

In this system $\alpha = \frac{1}{\delta t} + \frac{2}{Re}(\frac{1}{\delta x} + \frac{1}{\delta y})$ and the other quantities of the linear operator are relaxed in the second member. So $(D_h^{n-1})_{i-\frac{1}{2},j}$ represents the sum of these relaxed terms and $(B_h^{n-1})_{i-\frac{1}{2},j}$. We solve this 5×5 coupled system directly by a direct method. Indeed, eliminating the first four unknowns in the first four equations we get $p_{i,j}^n$, then the other unknowns follow. Let us point out that the fifth equation ensures the free divergence constraint in each cell.

4. Discretization of convection terms

The direct numerical simulation of high Reynolds number flows requires in particular a good approximation of convection terms. The challenge is to find out a scheme that ensures both accuracy and stability. Many works have dealt with this problem in the last two decades and with finite differences it appears that a good choice is to take a third-order scheme (see for instance [16]). Indeed, the stability of first-order schemes is very good, but their accuracy is poor as they induce a lot of diffusion. On the contrary, second-order schemes are more accurate but their stability is in general not ensured. In any cases, low order schemes neither capture the small eddies in the boundary layer nor convey properly the coherent structures. A way to improve the resolution of the method is to construct a high accurate scheme which holds good stability properties.

We first present or recall some third-order schemes for a non-linear convection equation constructed with the help of Euler scheme. Considering the one dimensional convection equation

$$\partial_t u(t,x) + \partial_x f(u(t,x)) = 0, \ t > 0, \ x \in \mathbb{R} \tag{4}$$

we denote $a(u) = f'(u)$, λ the ratio $\frac{\delta t}{\delta x}$ and u_i^n the numerical approximation of $u(n\delta t, i\delta x)$.

The well known first-order Murman scheme reads

$$u_i^{n+1} = u_i^n - \lambda\left(a_{i-\frac{1}{2}}^n\right)^+ (u_i^n - u_{i-1}^n) - \lambda\left(a_{i+\frac{1}{2}}^n\right)^- (u_{i+1}^n - u_i^n) \tag{5}$$

where $a^+ = \max(a,0)$; $a^- = \min(a,0)$ and

$$a_{i+\frac{1}{2}}^n = \begin{cases} \frac{f(u_{i+1}^n) - f(u_i^n)}{u_{i+1}^n - u_i^n} & \text{if } u_{i+1}^n \neq u_i^n \\ f'(u_i^n) & \text{if } u_{i+1}^n = u_i^n. \end{cases}$$

This scheme is stable, TVD and conservative. The disadvantage of this scheme is to introduce a lot of numerical diffusion. In fact, by Taylor series expansion at a generic point (t,x)

$$\frac{u(t+\delta t,x) - u(t,x)}{\delta t} = \partial_t u(t,x) + \frac{\delta t}{2}\partial_{tt} u(t,x) + \frac{\delta t^2}{6}\partial_{ttt} u(t,x) + \mathrm{O}(\delta t^3) \tag{6}$$

and

$$\frac{f(t,x) - f(t,x-\delta x)}{\delta x} = \partial_x f(t,x) - \frac{\delta x}{2}\partial_{xx} f(t,x) + \frac{\delta x^2}{6}\partial_{xxx} f(t,x) + \mathrm{O}(\delta x^3) \tag{7}$$

one gets, when f is a monotonous increasing function, that the first-order Murman scheme is a second-order approximation in time and space of the following convection–diffusion equation

$$\partial_t u(t,x) + \partial_x f(u(t,x)) - \frac{\delta x}{2}\partial_x((1 - \lambda a(u))\partial_x f(u))(t,x) = 0$$

To improve the approximation in time, it is possible to use Gear scheme or Runge–Kutta methods for instance. Another way is to keep Euler scheme in time and use Lax–Wendroff process to get high order schemes. In this case, one has to express the time derivatives in (6) by space derivatives of the flux using Eq. (4). After Lax and Wendroff, this idea was used to construct a third-order scheme for the advection equation [21] and gives rise to the famous Quickest scheme [16] which is based on upwind biases cubic interpolation. This scheme reads in conservative form

$$u_i^{n+1} = u_i^n - \lambda\left(a_{i+\frac{1}{2}}^n \phi_{i+\frac{1}{2}}^{(2)} - a_{i-\frac{1}{2}}^n \phi_{i-\frac{1}{2}}^{(2)}\right) - \lambda\left(a_{i+\frac{1}{2}}^n \phi_{i+\frac{1}{2}}^{(3)} - a_{i-\frac{1}{2}}^n \phi_{i-\frac{1}{2}}^{(3)}\right) \tag{8}$$

where $\phi_{i+\frac{1}{2}}^{(2)}$ represents the second-order Lax–Wendroff part

$$\phi_{i+\frac{1}{2}}^{(2)} = \frac{1}{2}\left((u_{i+1}^n + u_i^n) - \lambda a_{i+\frac{1}{2}}^n (u_{i+1}^n - u_i^n)\right)$$

and $\phi_{i+\frac{1}{2}}^{(3)}$ the third-order part

$$\phi_{i+\frac{1}{2}}^{(3)} = \frac{\left(1 - \left(\lambda a_{i+\frac{1}{2}}^n\right)^2\right)}{12}\left(u_{i+2}^n - u_{i+1}^n - u_i^n - u_{i-1}^n - sign\left(a_{i+\frac{1}{2}}^n\right)(u_{i+2}^n - 3u_{i+1}^n + 3u_i^n - u_{i-1}^n)\right)$$

$$= \begin{cases} \dfrac{\left(1 - \left(\lambda a_{i+\frac{1}{2}}^n\right)^2\right)}{6}(u_{i+1}^n - 2u_i^n + u_{i-1}^n) & \text{if } a_{i+\frac{1}{2}}^n > 0 \\ \dfrac{\left(1 - \left(\lambda a_{i+\frac{1}{2}}^n\right)^2\right)}{6}(u_{i+2}^n - 2u_{i+1}^n + u_i^n) & \text{otherwise} \end{cases}$$

However, this procedure is quite difficult to handle for the full Navier–Stokes equations without using a splitting method.

We now propose some schemes which use only a third-order approximation in space. To obtain a better approximation in time we can use for instance a Gear scheme as proposed in Section 2.2. When f is a monotonous increasing function, we propose a third-order Murman-like scheme that consists in using centered finite differences to approach $\partial_{xx} f$ and upwind differences to approach $\partial_{xxx} f$ in (7). The resulting scheme reads

$$u_i^{n+1} = u_i^n - \lambda \Delta_{i-\frac{1}{2}} f^n - \frac{\lambda}{2}(\Delta_{i+\frac{1}{2}} f^n - \Delta_{i-\frac{1}{2}} f^n) + \frac{\lambda}{6}(\Delta_{i+\frac{1}{2}} f^n - 2\Delta_{i-\frac{1}{2}} f^n + \Delta_{i-\frac{3}{2}} f^n) \tag{9}$$

where $\Delta_{i-\frac{1}{2}} f = f_i - f_{i-1}$.

When Eq. (4) has a meaning in non-conservative form

$$\partial_t u(t,x) + a(u)\partial_x u(t,x) = 0,\ t > 0,\ x \in \mathbb{R} \tag{10}$$

it is possible to give a non-conservative version of the previous schemes. In particular the third-order present scheme becomes

$$\begin{aligned} u_i^{n+1} = u_i^n & \\ & - \frac{1}{3}\lambda a_{i+\frac{1}{2}}^n \Delta_{i+\frac{1}{2}} u^n - \frac{5}{6}\lambda a_{i-\frac{1}{2}}^n \Delta_{i-\frac{1}{2}} u^n + \frac{1}{6}\lambda a_{i-\frac{3}{2}}^n \Delta_{i-\frac{3}{2}} u^n \quad \text{if } a_{i-\frac{1}{2}}^n > 0 \\ & - \frac{1}{3}\lambda a_{i-\frac{1}{2}}^n \Delta_{i-\frac{1}{2}} u^n - \frac{5}{6}\lambda a_{i+\frac{1}{2}}^n \Delta_{i+\frac{1}{2}} u^n + \frac{1}{6}\lambda a_{i+\frac{3}{2}}^n \Delta_{i+\frac{3}{2}} u^n \quad \text{if } a_{i+\frac{1}{2}}^n < 0 \end{aligned} \tag{11}$$

Note that if $a^n_{i-\frac{1}{2}} > 0$ and $a^n_{i+\frac{1}{2}} < 0$ the contribution of each term are added. In [13], Kawamura et al. propose a third-order upwind scheme which can be written explicitly in non-conservative form as

$$u_i^{n+1} = u_i^n - \begin{cases} \frac{\lambda}{6}a(u_i^n)(u^n_{i+2} - 2u^n_{i+1} + 9u^n_i - 10u^n_{i-1} + 2u^n_{i-2}) & \text{if } a(u_i^n) > 0 \\ -\frac{\lambda}{6}a(u_i^n)(u^n_{i-2} - 2u^n_{i-1} + 9u^n_i - 10u^n_{i+1} + 2u^n_{i+2}) & \text{otherwise} \end{cases} \tag{12}$$

This scheme is different from the standard third-order upwind scheme which uses a non-centered stencil

$$u_i^{n+1} = u_i^n - \begin{cases} \frac{\lambda}{6}a(u_i^n)(2u^n_{i+1} + 3u^n_i - 6u^n_{i-1} + u^n_{i-2}) & \text{if } a(u_i^n) > 0 \\ -\frac{\lambda}{6}a(u_i^n)(2u^n_{i-1} + 3u^n_i - 6u^n_{i+1} + u^n_{i+2}) & \text{otherwise} \end{cases} \tag{13}$$

These non-conservative schemes can be applied directly to the full Navier–Stokes equations. We illustrate below the four third-order schemes on the discretization of the term $-v^{n-1}\partial_y u^{n-1}$ in the second member at point $(i-\frac{1}{2}, j)$ (see Fig. 1).

Present

$$-\frac{1}{3}v^{n-1}_{i-\frac{1}{2},j+\frac{1}{2}}\frac{\Delta_{i-\frac{1}{2},j+\frac{1}{2}}u^{n-1}}{\delta y} - \frac{5}{6}v^{n-1}_{i-\frac{1}{2},j-\frac{1}{2}}\frac{\Delta_{i-\frac{1}{2},j-\frac{1}{2}}u^{n-1}}{\delta y} + \frac{1}{6}v^{n-1}_{i-\frac{1}{2},j-\frac{3}{2}}\frac{\Delta_{i-\frac{3}{2},j-\frac{3}{2}}u^{n-1}}{\delta y} \quad \text{if } v^{n-1}_{i-\frac{1}{2},j-\frac{1}{2}} > 0$$

$$-\frac{1}{3}v^{n-1}_{i-\frac{1}{2},j-\frac{1}{2}}\frac{\Delta_{i-\frac{1}{2},j-\frac{1}{2}}u^{n-1}}{\delta y} - \frac{5}{6}v^{n-1}_{i-\frac{1}{2},j+\frac{1}{2}}\frac{\Delta_{i-\frac{1}{2},j+\frac{1}{2}}u^{n-1}}{\delta y} + \frac{1}{6}v^{n-1}_{i-\frac{1}{2},j+\frac{3}{2}}\frac{\Delta_{i-\frac{3}{2},j+\frac{3}{2}}u^{n-1}}{\delta y} \quad \text{if } v^{n-1}_{i-\frac{1}{2},j+\frac{1}{2}} < 0$$

Upwind 3

$$\begin{cases} -v^{n-1}_{i-\frac{1}{2},j}\left(\frac{1}{3}u^{n-1}_{i-\frac{1}{2},j+1} + \frac{1}{2}u^{n-1}_{i-\frac{1}{2},j} - u^{n-1}_{i-\frac{1}{2},j-1} + \frac{1}{6}u^{n-1}_{i-\frac{1}{2},j-2}\right)/\delta y & \text{if } v^{n-1}_{i-\frac{1}{2},j} > 0 \\ v^{n-1}_{i-\frac{1}{2},j}\left(\frac{1}{3}u^{n-1}_{i-\frac{1}{2},j-1} + \frac{1}{2}u^{n-1}_{i-\frac{1}{2},j} - u^{n-1}_{i-\frac{1}{2},j+1} + \frac{1}{6}u^{n-1}_{i-\frac{1}{2},j+2}\right)/\delta y & \text{otherwise} \end{cases}$$

where $v^{n-1}_{i-\frac{1}{2},j} = \frac{1}{4}\left(v^{n-1}_{i-1,j-\frac{1}{2}} + v^{n-1}_{i-1,j+\frac{1}{2}} + v^{n-1}_{i,j-\frac{1}{2}} + v^{n-1}_{i,j+\frac{1}{2}}\right)$.

Kawamura

$$\begin{cases} -v^{n-1}_{i-\frac{1}{2},j}\left(\frac{1}{6}u^{n-1}_{i-\frac{1}{2},j+2} - \frac{1}{3}u^{n-1}_{i-\frac{1}{2},j+1} + \frac{3}{2}u^{n-1}_{i-\frac{1}{2},j} - \frac{5}{3}u^{n-1}_{i-\frac{1}{2},j-1} + \frac{1}{3}u^{n-1}_{i-\frac{1}{2},j-2}\right)/\delta y & \text{if } v^{n-1}_{i-\frac{1}{2},j} > 0 \\ v^{n-1}_{i-\frac{1}{2},j}\left(\frac{1}{6}u^{n-1}_{i-\frac{1}{2},j-2} - \frac{1}{3}u^{n-1}_{i-\frac{1}{2},j-1} + \frac{3}{2}u^{n-1}_{i-\frac{1}{2},j} - \frac{5}{3}u^{n-1}_{i-\frac{1}{2},j+1} + \frac{1}{3}u^{n-1}_{i-\frac{1}{2},j+2}\right)/\delta y & \text{otherwise} \end{cases}$$

Quickest

$$-\frac{1}{2\delta y}v^{n-1}_{i-\frac{1}{2},j+\frac{1}{2}}\left(u^{n-1}_{i-\frac{1}{2},j+1} + u^{n-1}_{i-\frac{1}{2},j} - \frac{\delta t}{\delta y}v^{n-1}_{i-\frac{1}{2},j+\frac{1}{2}}\left(u^{n-1}_{i-\frac{1}{2},j+1} - u^{n-1}_{i-\frac{1}{2},j}\right)\right)$$

$$+\frac{1}{2\delta y}v^{n-1}_{i-\frac{1}{2},j-\frac{1}{2}}\left(u^{n-1}_{i-\frac{1}{2},j} + u^{n-1}_{i-\frac{1}{2},j-1} - \frac{\delta t}{\delta y}v^{n-1}_{i-\frac{1}{2},j-\frac{1}{2}}\left(u^{n-1}_{i-\frac{1}{2},j} - u^{n-1}_{i-\frac{1}{2},j-1}\right)\right)$$

$$-\frac{1}{6\delta y}v^{n-1}_{i-\frac{1}{2},j+\frac{1}{2}}\begin{cases}\left(1-\left(\frac{\delta t}{\delta y}v^{n-1}_{i-\frac{1}{2},j+\frac{1}{2}}\right)^2\right)\left(u^{n-1}_{i-\frac{1}{2},j+1}-2u^{n-1}_{i-\frac{1}{2},j}+u^{n-1}_{i-\frac{1}{2},j-1}\right) & \text{if } v^{n-1}_{i-\frac{1}{2},j+\frac{1}{2}}>0\\ \left(1-\left(\frac{\delta t}{\delta y}v^{n-1}_{i-\frac{1}{2},j+\frac{1}{2}}\right)^2\right)\left(u^{n-1}_{i-\frac{1}{2},j+2}-2u^{n-1}_{i-\frac{1}{2},j+1}+u^{n-1}_{i-\frac{1}{2},j}\right) & \text{otherwise}\end{cases}$$

$$+\frac{1}{6\delta y}v^{n-1}_{i-\frac{1}{2},j-\frac{1}{2}}\begin{cases}\left(1-\left(\frac{\delta t}{\delta y}v^{n-1}_{i-\frac{1}{2},j-\frac{1}{2}}\right)^2\right)\left(u^{n-1}_{i-\frac{1}{2},j}-2u^{n-1}_{i-\frac{1}{2},j-1}+u^{n-1}_{i-\frac{1}{2},j-2}\right) & \text{if } v^{n-1}_{i-\frac{1}{2},j-\frac{1}{2}}>0\\ \left(1-\left(\frac{\delta t}{\delta y}v^{n-1}_{i-\frac{1}{2},j-\frac{1}{2}}\right)^2\right)\left(u^{n-1}_{i-\frac{1}{2},j+1}-2u^{n-1}_{i-\frac{1}{2},j}+u^{n-1}_{i-\frac{1}{2},j-1}\right) & \text{otherwise}\end{cases}$$

To take into account the boundary conditions, we use two fictitious cells out side of the domain where the velocity is linearly extrapolated according to its value at the boundary.

5. Numerical comparison on steady solutions

In this section, we compare the previous schemes on steady solutions for which an abundant literature is available. First results were already given about 20 years ago in [8,20]. Since then, many authors compared their results to these pioneer works. The results presented in this section are computed with Euler scheme in time whatever the space discretization is for convection terms. Indeed, as the solution is steady, the time scheme has no influence on the accuracy of the final solution. These solutions are qualified as steady when the relative error between two time steps is less than 10^{-12} on a significant time interval. This steady property is also seen on the velocity or pressure signals at monitoring points that are constant and on the phase portraits that reduce to a single point.

5.1. The $Re = 1000$ lid driven cavity flow

The first classical test case we consider is the cavity flow at $Re = 1000$. Recently, an accurate study has been performed using a Chebyshev collocation method [3] for this test case. They obtain a good convergence up to seven digits on two consecutive approximations. Numerous comparisons with other results of the literature can be found in this paper. The solution computed with our method is plotted in Fig. 2. It exhibits a large primary vortex with two secondary vortices in the two bottom corners. The pressure isolines are plotted after setting the pressure equal to zero at the center of the cavity. The values of the stream-function, the vorticity and the pressure contours are given in Table 1. As in [3], the value 0.1175 of the stream-function is chosen to better represent the primary vortex core. The plain isolines refer to positive values and the dotted isolines refer to non-positive values.

First of all, we give comparisons in Tables 2 and 3 of the four different third-order schemes presented in Section 4. They concern the value and the location of the extrema of the stream-function to which is added the value of the vorticity at the same location. The choice of these values is governed by the data available in the literature. We can see on these tables that three schemes give

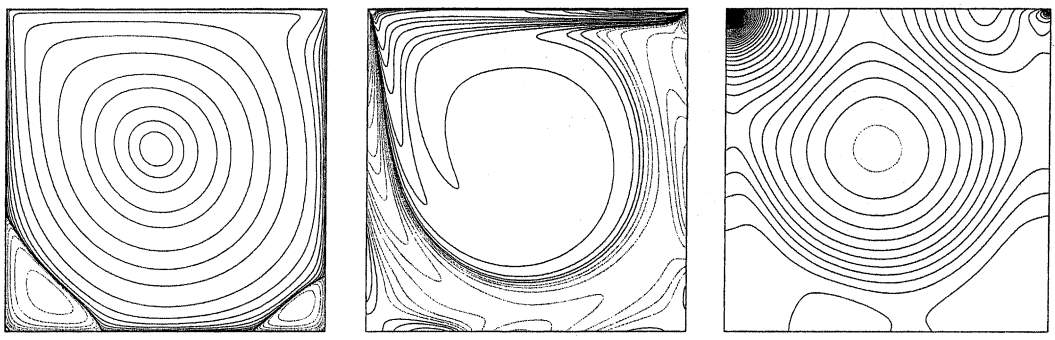

Fig. 2. Steady solution at $Re = 1000$ computed with present scheme on grid 1024×1024. From left to right stream-function, vorticity and pressure fields.

Table 1
Contours values of the stream-function, the vorticity and the pressure

Isolines values					
Stream-function					
-0.1	-0.08	-0.06	-0.04	-0.02	-0.01
-3×10^{-3}	-1×10^{-3}	-3×10^{-4}	-1×10^{-4}	-3×10^{-5}	-1×10^{-5}
-3×10^{-6}	-1×10^{-6}	-1×10^{-7}	-1×10^{-8}	-1×10^{-9}	-1×10^{-10}
0.0	1×10^{-10}	1×10^{-9}	1×10^{-8}	1×10^{-7}	1×10^{-6}
3×10^{-6}	1×10^{-5}	3×10^{-5}	1×10^{-4}	3×10^{-4}	1×10^{-3}
3×10^{-3}	0.01	0.03	0.05	0.07	0.09
0.1	0.11	0.115	0.1175		
Vorticity					
-40.0	-35.0	-30.0	-25.0	-20.0	-15.0
-10.0	-8.0	-6.0	-4.0	-3.0	-2.0
-1.0	-0.5	-0.2	0.2	0.5	1.0
2.0	3.0	4.0	6.0	8.0	10.0
15.0	20.0	25.0	30.0	35.0	40.0
Pressure	from -2.0 to 2.0 by step 0.01				

about the same values on a sequence of grids but not the Quickest scheme [16] which is far too diffusive. Among the three others, the scheme proposed by Kawamura et al. is less stable than the two others. Indeed it requires a CFL condition more restrictive. For instance on the grid 128×128 the time step $\delta t = 0.006$ is needed instead of $\delta t = 0.008$. This is not surprising because this scheme uses a centered stencil and is in some sense more centered than the others. The CFL condition imposed by the explicit treatment of convection terms gives $\delta t = 0.0078125$. Then this scheme needs a CFL number around 0.75 when the others accept a CFL number slightly greater than one. Then we compare our results to these of the literature and plot the same data in Table 4. We compare, on one hand, on a coarse grid to the classical results in [8,20,22] and on the other hand on a fine grid to the very accurate results obtained in [3] with 160 Chebyshev

Table 2
Comparison of the four third-order schemes on the primary vortex at $Re = 1000$: maximum of the stream-function, vorticity and location

Scheme	Grid	ψ_{max}	ω	x	y
Present	128×128	0.11786	2.0508	0.46875	0.5625
Upwind 3	128×128	0.11796	2.0549	0.46875	0.5625
Kawamura	128×128	0.11790	2.0557	0.46875	0.5625
Quickest	128×128	0.11503	1.9910	0.46875	0.5625
Present	256×256	0.11865	2.0634	0.46875	0.5664
Upwind 3	256×256	0.11870	2.0644	0.46875	0.5664
Kawamura	256×256	0.11867	2.0636	0.46875	0.5664
Quickest	256×256	0.11599	2.0069	0.46875	0.5664
Present	512×512	0.11886	2.0665	0.46875	0.56445
Upwind 3	512×512	0.11887	2.0668	0.46875	0.56445
Kawamura	512×512	0.11887	2.0667	0.46875	0.56445
Quickest	512×512	0.11741	2.0350	0.46875	0.56445
Present	1024×1024	0.11892	2.0674	0.46875	0.56543
Upwind 3	1024×1024	0.11892	2.0674	0.46875	0.56445
Kawamura	1024×1024	0.11892	2.0674	0.46875	0.56445
Quickest	1024×1024	0.11798	2.0434	0.46875	0.56445

Table 3
Comparison of the four third-order schemes on the lower left secondary vortex at $Re = 1000$: minimum of the stream-function, vorticity and location

Scheme	Grid	ψ_{min}	ω	x	y
Present	128×128	-1.7003×10^{-3}	-1.1304	0.14063	0.10938
Upwind 3	128×128	-1.7322×10^{-3}	-1.1204	0.14063	0.10938
Kawamura	128×128	-1.7281×10^{-3}	-1.1138	0.14063	0.10938
Quickest	128×128	-1.7689×10^{-3}	-1.0771	0.13281	0.10938
Present	256×256	-1.7219×10^{-3}	-1.1345	0.13672	0.11328
Upwind 3	256×256	-1.7303×10^{-3}	-1.1333	0.13672	0.11328
Kawamura	256×256	-1.7295×10^{-3}	-1.1322	0.13672	0.11328
Quickest	256×256	-1.7551×10^{-3}	-1.1340	0.13672	0.10938
Present	512×512	-1.7279×10^{-3}	-1.1137	0.13672	0.11133
Upwind 3	512×512	-1.7300×10^{-3}	-1.1132	0.13672	0.11133
Kawamura	512×512	-1.7299×10^{-3}	-1.1131	0.13672	0.11133
Quickest	512×512	-1.7419×10^{-3}	-1.1082	0.13477	0.11133
Present	1024×1024	-1.7292×10^{-3}	-1.1120	0.13574	0.11230
Upwind 3	1024×1024	-1.7297×10^{-3}	-1.1143	0.13672	0.11133
Kawamura	1024×1024	-1.7297×10^{-3}	-1.1143	0.13672	0.11133
Quickest	1024×1024	-1.7333×10^{-3}	-1.1265	0.13672	0.11133

polynomials. We can see that the present results compare very well and that the results on the medium grids are already very good.

Table 4
Comparison of various works on the primary vortex and on the lower left secondary vortex at $Re = 1000$

Scheme	Grid	ψ_{max}	ω	x	y
Present	128×128	0.11786	2.0508	0.46875	0.5625
Ghia [8]	128×128	0.117929	2.04968	0.4687	0.5625
Schreiber [20]	140×140	0.11603	2.026	0.47143	0.56429
Vanka [22]	320×320	0.1173	–	0.4562	0.5625
Present	1024×1024	0.11892	2.0674	0.46875	0.56543
Botella [3]	$N = 160$	0.1189366	2.067753	0.4692	0.5652
		ψ_{min}			
Present	128×128	-1.7003×10^{-3}	−1.1304	0.14063	0.10938
Ghia [8]	128×128	-1.75102×10^{-3}	−1.15465	0.14062	0.1094
Schreiber [20]	140×140	-1.700×10^{-3}	−0.999	0.13571	0.10714
Vanka [22]	320×320	-1.74×10^{-3}	–	0.1375	0.1063
Present	1024×1024	-1.7292×10^{-3}	−1.1120	0.13672	0.11230
Botella [3]	$N = 160$	-1.729717×10^{-3}	−1.109789	0.13602	0.1118

Some other quantities are available in the literature. In particular the velocity, the pressure and the vorticity along the centerlines of the cavity. Once again, we can see in Tables 5 and 6 that the present results are in very good agreement with the results found in [3].

Finally, we think that in addition to local quantities it is interesting to compare global quantities as the total kinetic energy E, the enstrophy Z and the palinstrophy P defined by

$$E = \frac{1}{2}\int_\Omega \|U\|^2 \mathrm{d}x, \quad Z = \frac{1}{2}\int_\Omega \|\omega\|^2 \mathrm{d}x, \quad P = \frac{1}{2}\int_\Omega \|\nabla\omega\|^2 \mathrm{d}x$$

where $\omega = \partial_x v - \partial_y u$ is the vorticity. Denoting $U_{i,j} = (u_{i,j}, v_{i,j}) = \left(\left(u_{i+\frac{1}{2},j} + u_{i-\frac{1}{2},j}\right)\Big/2, \left(v_{i,j+\frac{1}{2}} + v_{i,j-\frac{1}{2}}\right)\Big/2\right)$ the velocity at the center of a cell, the energy is approximated by

$$\frac{1}{2}\delta x \delta y \sum_{i,j}(u_{i,j}^2 + v_{i,j}^2)$$

Table 5
Horizontal velocity, pressure and vorticity through the vertical centerline of the cavity at $Re = 1000$ with the present scheme on grid 1024×1024

y	u, Ref. [8]	u, Ref. [3]	u, Present	p, Ref. [3]	p, Present	ω, Ref. [3]	ω, Present
1.0000	−1.00000	−1.00000	−1.00000	0.052987	0.052971	14.7534	14.792
0.9688	−0.57492	−0.58083	−0.58031	0.051514	0.051493	9.49496	9.4781
0.9531	−0.46604	−0.47233	−0.47239	0.050329	0.050314	4.85754	4.8628
0.7344	−0.18719	−0.18867	−0.18861	0.012122	0.012113	2.09121	2.0909
0.5000	0.06080	0.06205	0.06205	0.000000	0.000000	2.06722	2.0669
0.2813	0.27805	0.28036	0.28040	0.040377	0.040381	2.26722	2.2678
0.1016	0.29730	0.30045	0.30029	0.104187	0.104416	−1.63436	−1.6352
0.0625	0.20196	0.20233	0.20227	0.109200	0.10916	−2.31786	−2.3174
0.0000	0.00000	0.00000	0.00000	0.110591	0.11056	−4.16648	−4.1554

Table 6
Vertical velocity, pressure and vorticity through the horizontal centerline of the cavity at $Re = 1000$ with the present scheme on grid 1024×1024

x	v, Ref. [8]	v, Ref. [3]	v	p, Ref. [3]	p	ω, Ref. [3]	ω
0.0000	0.00000	0.00000	0.00000	0.077455	0.077429	−5.46217	−5.4967
0.0391	−0.27669	−0.29368	−0.29330	0.078685	0.078658	−8.24616	−8.2462
0.0547	−0.39188	−0.41037	−0.41018	0.077154	0.077128	−6.50867	−6.5097
0.1406	−0.42665	−0.42645	−0.42634	0.049029	0.049004	3.43016	3.4294
0.5000	0.02526	0.02579	0.02580	0.000000	0.00000	2.06722	2.0669
0.7734	0.33075	0.33399	0.33398	0.047260	0.047259	2.00174	2.0010
0.9062	0.32627	0.33304	0.33290	0.084386	0.084369	−0.82398	−0.82517
0.9297	0.29012	0.29627	0.29622	0.087653	0.087625	−1.50306	−1.5025
1.0000	0.00000	0.00000	0.00000	0.090477	0.090448	−7.66369	−7.6333

The other quantities are computed in the same way with the vorticity evaluated at the vertices of the mesh and its gradient at the middle of the cell sides. As the solution is stationary, these quantities yield a constant value which is about the same for the three first schemes as shown in Table 7. We can see that the grid convergence is achieved for the kinetic energy whereas it is false for the two other quantities. Indeed for this problem, because of the singularity at the corner, it is not possible to get convergence as there is a jump of the velocity that induces infinite derivatives. It is well known that the enstrophy behaves like $1/r$ near the singular corners [2,3] and thus the enstrophy and palinstrophy go to infinity as the mesh size goes to zero. The same quantities

Table 7
Comparison of the four third-order schemes on the global quantities energy, enstrophy and palinstrophy at $Re = 1000$

Scheme	Grid	Energy	Enstophy	Palinstrophy
Present	128×128	0.043641	17.567	$0.14377 \times 10^{+6}$
Upwind 3	128×128	0.043721	17.685	$0.15280 \times 10^{+6}$
Kawamura	128×128	0.043672	17.634	$0.14815 \times 10^{+6}$
Quickest	128×128	0.041973	17.394	$0.14462 \times 10^{+6}$
Present	256×256	0.044286	19.328	$0.48476 \times 10^{+6}$
Upwind 3	256×256	0.044313	19.363	$0.49696 \times 10^{+6}$
Kawamura	256×256	0.044300	19.348	$0.49253 \times 10^{+6}$
Quickest	256×256	0.042690	19.159	$0.48594 \times 10^{+6}$
Present	512×512	0.044458	20.908	$0.17708 \times 10^{+7}$
Upwind 3	512×512	0.044466	20.918	$0.17862 \times 10^{+7}$
Kawamura	512×512	0.044463	20.915	$0.17831 \times 10^{+7}$
Quickest	512×512	0.043580	20.818	$0.17749 \times 10^{+7}$
Present	1024×1024	0.044503	22.424	$0.68169 \times 10^{+7}$
Upwind 3	1024×1024	0.044500	22.426	$0.68358 \times 10^{+7}$
Kawamura	1024×1024	0.044500	22.425	$0.68343 \times 10^{+7}$
Quickest	1024×1024	0.043967	22.374	$0.68260 \times 10^{+7}$

computed for the regularized cavity problem with $U(t,x,1) = (-16x^2(1-x)^2, 0)$ gives converged values as can be seen in Table 8.

Table 8
Convergence of the total quantities for the regularized cavity problem at $Re = 1000$

Scheme	Grid	Energy	Enstophy	Palinstrophy
Present	64×64	0.021564	4.6458	$0.56113 \times 10^{+4}$
Present	128×128	0.022315	4.7711	$0.70138 \times 10^{+4}$
Present	256×256	0.022542	4.8123	$0.78165 \times 10^{+4}$
Present	512×512	0.022607	4.8243	$0.82699 \times 10^{+4}$

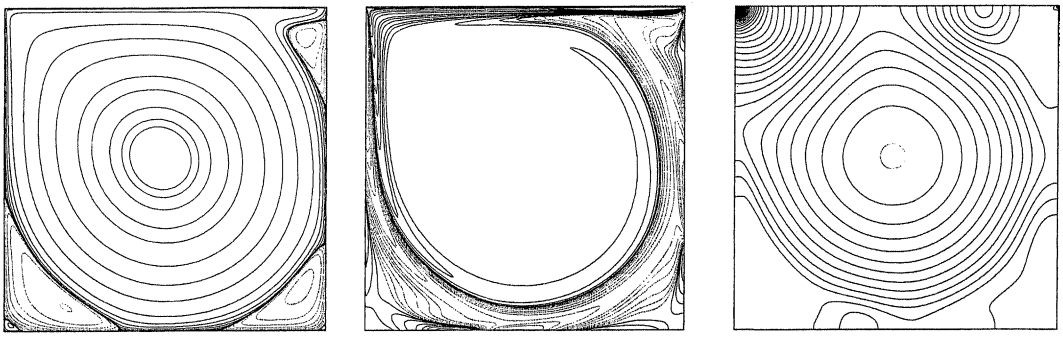

Fig. 3. Steady solution at $Re = 5000$ computed with present scheme on grid 2048×2048. Erom left to right stream-function, vorticity and pressure fields.

Table 9
Comparison of the four third-order schemes on the primary vortex at $Re = 5000$: maximum of the stream-function, vorticity and location

Scheme	Grid	$\psi_{\max}$	ω	x	y
Present	128×128	0.11731	1.8595	0.48438	0.53906
Upwind 3	128×128	0.11755	1.9797	0.48438	0.53906
Kawamura	128×128	0.11795	1.8938	0.48438	0.53906
Quickest	128×128	0.10889	1.6967	0.48438	0.53906
Present	256×256	0.12064	1.9125	0.48438	0.53516
Upwind 3	256×256	0.12085	1.9196	0.48438	0.53516
Kawamura	256×256	0.12097	1.9219	0.48438	0.53516
Quickest	256×256	0.11331	1.7706	0.48438	0.53516
Present	512×512	0.12173	1.9299	0.48438	0.53516
Upwind 3	512×512	0.12182	1.9327	0.48438	0.53516
Kawamura	512×512	0.12182	1.9331	0.48438	0.53516
Quickest	512×512	0.11710	1.8351	0.48438	0.53516
Present	1024×1024	0.12193	1.9322	0.48535	0.53516
Upwind 3	1024×1024	0.12200	1.9343	0.48535	0.53516

5.2. The $Re = 5000$ lid driven cavity flow

This Reynolds number $Re = 5000$ is a good choice as there are some comparisons available in the literature and as the steady solution is still stable but not too far from the first Hopf bifurcation. For this test case, there is no very accurate results as in the previous case and we choose our results obtained with the present scheme on a fine grid 2048×2048 as a reference. This solution is

Table 10
Comparison of the four third-order schemes on the lower left secondary vortex at $Re = 5000$: minimum of the stream-function, vorticity and location

Scheme	Grid	$\psi_{\min}$	ω	x	y
Present	128×128	-2.9313×10^{-3}	-2.7718	0.19531	0.070313
Upwind 3	128×128	-3.0228×10^{-3}	-2.4974	0.19531	0.078125
Kawamura	128×128	-2.9790×10^{-3}	-2.4705	0.19531	0.078125
Quickest	128×128	-3.7090×10^{-3}	-3.4205	0.19531	0.070313
Present	256×256	-3.0348×10^{-3}	-2.6330	0.19141	0.074219
Upwind 3	256×256	-3.0630×10^{-3}	-2.6810	0.19531	0.074219
Kawamura	256×256	-3.0573×10^{-3}	-2.6746	0.19531	0.074219
Quickest	256×256	-3.4009×10^{-3}	-3.1966	0.19531	0.070313
Present	512×512	-3.0618×10^{-3}	-2.7458	0.19531	0.072266
Upwind 3	512×512	-3.0708×10^{-3}	-2.7368	0.19531	0.072266
Kawamura	512×512	-3.0699×10^{-3}	-2.7355	0.19531	0.072266
Quickest	512×512	-3.2265×10^{-3}	-2.9918	0.19531	0.070313
Present	1024×1024	-3.0694×10^{-3}	-2.7245	0.19434	0.073242
Upwind 3	1024×1024	-3.0722×10^{-3}	-2.7735	0.19629	0.072266

Table 11
Comparison of various works on the primary vortex and on the lower left secondary vortex at $Re = 5000$

Scheme	Grid	$\psi_{\max}$	ω	x	y
Present	256×256	0.12064	1.9125	0.48438	0.53516
Ghia [8]	256×256	0.118966	1.86016	0.4883	0.5352
Huser [12]	80×80 stretched	0.1219	2.001	–	–
Kim-Moin [14]	96×96 stretched	0.112	1.812	–	–
Goodrich [10]	256×256	0.118	–	0.48438	0.53516
Vanka [22]	160×160	0.0920	–	0.4875	0.5313
Pan-Glowinski [17]	256×256	0.121218	–	0.4844	0.5352
Kupperman [15]	128×128	0.12216	–	–	–
Present (reference)	2048×2048	0.12197	1.9327	0.48535	0.53516
		$\psi_{\min}$			
Present	256×256	-3.0348×10^{-3}	-2.6330	0.19141	0.074219
Ghia [8]	256×256	-3.0835×10^{-3}	-2.66354	0.1914	0.07422
Goodrich [10]	256×256	-3.13×10^{-3}	–	0.1953	0.07422
Vanka [22]	160×160	-5.49×10^{-3}	–	0.15	0.0813
Present (reference)	2048×2048	-3.0706×10^{-3}	-2.7244	0.19434	0.073242

Table 12
Comparison of the four third-order schemes on the global quantities energy and enstrophy at $Re = 5000$

Scheme	Grid	Energy	Enstrophy
Present	128×128	0.043566	30.861
Upwind 3	128×128	0.043740	31.986
Kawamura	128×128	0.043874	30.601
Quickest	128×128	0.038563	29.535
Present	256×256	0.046204	34.368
Upwind 3	256×256	0.046353	34.851
Kawamura	256×256	0.046347	34.645
Quickest	256×256	0.041537	33.709
Present	512×512	0.047066	36.768
Upwind 3	512×512	0.047132	36.957
Kawamura	512×512	0.047126	36.890
Quickest	512×512	0.044084	36.325
Present	1024×1024	0.047255	38.643
Upwind 3	1024×1024	0.047292	38.698
Present	2048×2048	0.047290	40.261

plotted in Fig. 3. It exhibits in addition to the two secondary vortices in the bottom corners a third vortex in the upper right corner and much stronger gradients than the solution at $Re = 1000$.

We compare again the four third-order schemes at this Reynolds number. We can see in Tables 9 and 10 that the Quickest scheme is still too diffusive. We can also make the same remark about the stability for Kawamura et al. scheme that needs a CFL number 0.75. The two other schemes give close results. The comparison with the results of the literature (Table 11) is quite difficult as the results are most often given on a single grid. In [22] this is due to the lost of stability on finer grids. Nevertheless our results are coherent with the results given in [8,15,17,10]. The last point we present is the comparison of the global quantities energy and enstrophy. The grid convergence is reached for the kinetic energy and we can see in Table 12 that the upwind scheme and the present scheme give about the same results. The whole comparison in Sections 5.1 and 5.2 shows that the steady solutions we get are in very good agreement with the one of the literature and also shows that among the four third-order schemes the upwind scheme and the present scheme are the best. We choose to perform all the simulations to the end of the paper with our proposed scheme.

6. Linear stability

6.1. Linearized problem

In this section, we are studying the stability of the steady solution. We want to know as accurately as possible when the steady solution loses its stability to the benefit of a periodic solution, which corresponds to the localization of the first Hopf bifurcation. In other terms, how far a steady-state solution can be observed physically? To answer this question we propose to compute the

first Lyapunov exponent of the linearized system. As we are only interested in the first Hopf bifurcation, we assume that a small perturbation (V, q) is added to the steady solution (U_s, p_s) of system (1). The stability study consists in looking at the behaviour of the perturbation along time. This behaviour is driven by the smallest real part of the eigenvalues of the linearized space operator. If the steady solution is stable, the perturbation goes to zero when t goes to infinity as $e^{\mu_1 t}$ where μ_1 is the first Lyapunov exponent defined by (see [1]):

$$\mu_1 = \lim_{t \to +\infty} \frac{\mathrm{Log}\|V(t)\|}{t}$$

Using the fact that (U_S, p_S) is a steady solution, we have to solve the simplified linear problem

$$\begin{aligned} &\partial_t V - \frac{1}{Re}\Delta V + (U_S \cdot \nabla)V + (V \cdot \nabla)U_S + \nabla_q = 0 && \text{in } \Omega \times (0,T) \\ &\nabla \cdot V = 0 && \text{in } \Omega \times (0,T) \\ &V = V_0 && \text{in } \Omega \\ &V = 0 && \text{on } \partial\Omega \times (0,T) \end{aligned} \tag{14}$$

where the non-linear term $(V \cdot \nabla)V$ is neglected.

6.2. Steady solution analysis

The problem (14) is solved exactly in the same way that the initial problem (1). The only difficulty is that the numerical solution V^n at time $n\delta t$ becomes very small for large n. So, the solution is normalized at each time iteration by setting $V_0^n = V^n / \|V^{n-1}\|$ and the Lyapunov exponent is approximated by

$$\mu_1^n = \frac{\sum_{i=0}^{n-1} \mathrm{Log}\|V_0^i\|}{n\delta t}$$

if we take $\|V_0\| = 1$. The results are not very sensitive to the initial datum V_0. We can choose either an arbitrary datum satisfying the boundary conditions such that $\|V_0\| = 1$ or the difference between a periodic and a steady solution of (1) normalized to one.

The main difficulty is probably to well determine the convergence criteria. It appears that the behaviour of the sequence V^n is very different from low Reynolds numbers to high Reynolds numbers. At $Re = 10$ for instance, the norm of V^n decreases very fast and cannot be the unique criterion of convergence. Indeed, the value of the Lyapunov exponent can be very far to the converged value even if $\|V^n\| = 10^{-10}$. It is then necessary to add a crite rion based on the relative error on the approximation of μ_1. Conversely for Reynolds numbers higher than 5000 the norm of V^n decreases very slowly and the relative error is smaller than $\|V^n\|$. So, we decide to take two criteria for the convergence $\|V^n\| \leqslant 10^{-8}$ and $\|\mu_1^n - \mu_1^{n-1}\| / \|\mu_1^{n-1}\| \leqslant 10^{-6}$. We stop the computation only if the two criteria are satisfied.

Another important point is the computation of the steady solution (U_S, p_S) for high Reynolds numbers. It is absolutely necessary that the steady state has been completely achieved. On coarse grids, the solution with Euler scheme can be periodic and thus the linearized computation will fail

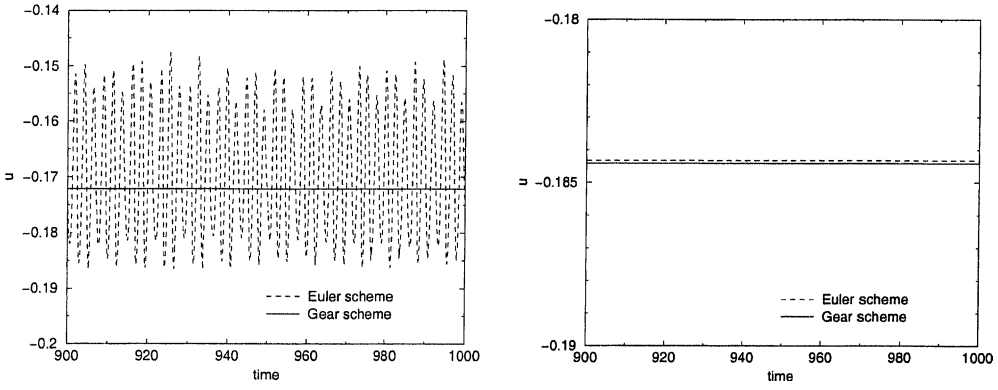

Fig. 4. Horizontal velocity history at monitoring point (14/16, 13/16) for $Re = 7800$. Comparison of Euler and Gear schemes on the 128×128 (left) and 256×256 (right) grids.

Table 13
Evolution of the Lyapunov exponent with Reynolds number

Re	10	100	1000	5000	7800	8000
T	38	110	242	1386	2243	7442
μ_1	−5.2	−0.56	−0.076	−0.013	−0.0082	−0.0026

(see Fig. 4). In this case, either the use of Gear scheme or a computation on a finer grid is necessary to reach the steady-state and insure the success of the convergence of V^n. The plots of Fig. 4 show that both choices are efficient. Until $Re = 8000$, we get a steady solution on grid 256×256 as well as on finer grids. For low Reynolds numbers the convergence to the Lyapunov exponent is very fast and monotonous. On the contrary, for high Reynolds numbers the convergence is very slow and not monotonous. Actually the sequence μ_1^n oscillates around the limit for a long time. For example at $Re = 8000$ the value $\mu_1 = -0.0026$ (see Table 13) is reached at time $T = 2400$

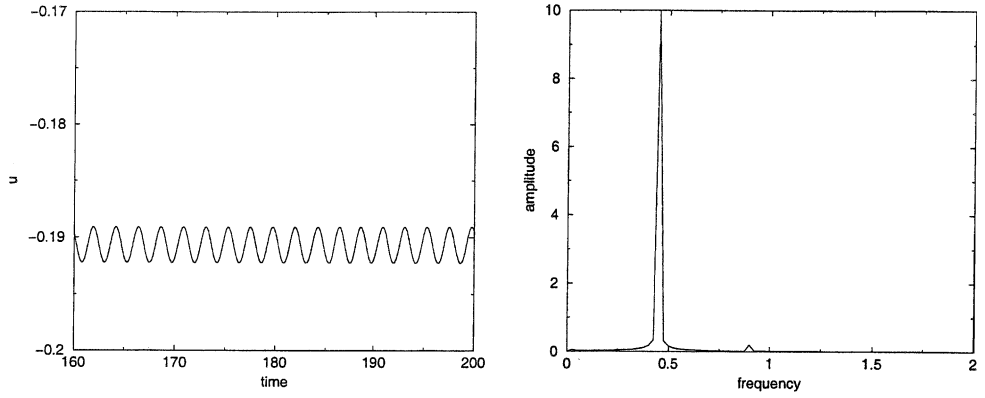

Fig. 5. Horizontal velocity history (left) and power spectrum (right) on grid 1024×1024 at monitoring point (14/16, 13/16) for $Re = 8050$. Computation with Gear scheme in time and present scheme in space.

and then μ_1^n oscillates slightly around this value. The fact that the first Lyapunov exponent goes to zero indicates that the steady solution looses its stability and that the critical Reynolds number is very close to $Re = 8000$. Moreover, the presence of the first Hopf bifurcation is confirmed by the computation of the solution of Navier–Stokes system which is stationary under this value and periodic beyond. The numerical approximation yields the stable solution whatever the initial datum is. Even starting with the steady solution obtained at $Re = 8000$, the convergence process for a simulation at $Re = 8050$ drifts slowly towards a stable periodic solution. Once again, we see the need of an accurate time scheme to get the right solution at $Re = 8050$. On grid 256×256 we get after a very long simulation time a steady solution with Euler scheme whereas we get a periodic solution with Gear scheme. But on grid 512×512 or on finer grids both time schemes give a periodic solution with the same frequency $f = 0.45$ (see Fig. 5). We can conclude from our numerical tests performed on several consecutive grids that the critical Reynolds number for the 2D lid-driven cavity problem is $8000 \leqslant R_c \leqslant 8050$ within less than 1% of error. The present value of the critical Reynolds number is also confirmed by the few results available in the literature, in particular in [7,19] where the first eigenvalues are computed. In these papers, the authors localize the first Hopf bifurcation at $Re = 7998.5$ or $Re = 8031.93$ when the eigenvalue with the smallest real part reaches the imaginary axis. In references [2,17,18] the critical Reynolds number is given respectively around $Re = 8018$, between $Re = 7500$ and $Re = 8500$ and around $Re = 7400$.

7. Periodic solutions

After the first Hopf bifurcation, there is a stable periodic solution. At $Re = 8100$, the solution computed on grid 512×512 with gear scheme in time and the present scheme in space is a purely periodic solution with frequency $f = 0.45$ as shown in Fig. 6. In this figure is plotted the time evolution of the first component of the velocity at monitoring point (14/16,13/16) and a Fourier analysis is performed for this signal. However the behaviour is exactly the same for other quantities as the pressure, the second component of the velocity or the vorticity. Moreover the same

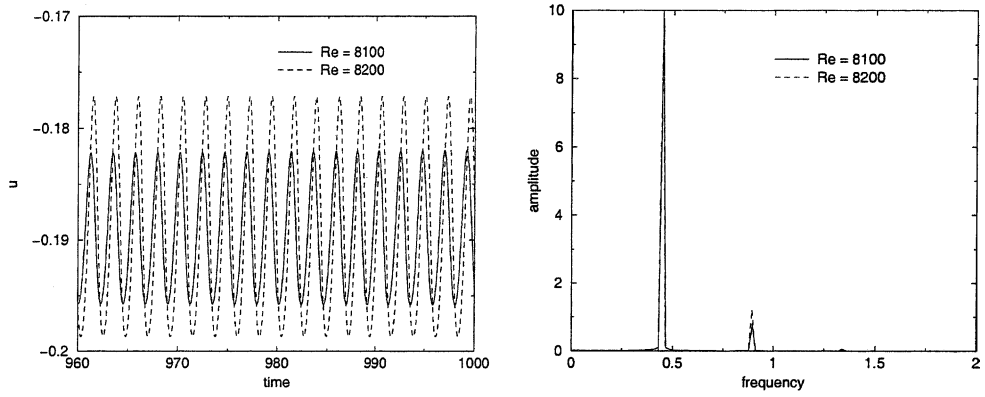

Fig. 6. Horizontal velocity history (left) and power spectrum (right) on grid 512×512 at monitoring point (14/16,13/16) for $Re = 8100$ and $Re = 8200$ Computation with Gear scheme in time and present scheme in space.

results are obtained at the other points considered, namely (1/2, 1/2), (1/16, 1/2), (3/16, 1/16), (14/16, 1/16) and (14/16, 15/16) even if there is some variations on the amplitude of the signals. These points are chosen in order to well analyze the behaviour of the solution in every part of the cavity. For $Re = 8200$ a good periodic solution is obtained with the same frequency (see Fig. 6). Let us point out to the reader that for these Reynolds numbers the grid convergence is achieved as the solutions on two consecutive grids 512×512 and 1024×1024 are identical. In addition the frequency is very close to the one obtained at $Re = 8000$ in [7], $Re = 8018$ in [2] and $Re = 8500$ in [17].

Then we compute the solution at $Re = 10{,}000$. This value is probably the most famous value and for quite a long time the question was to know if the steady solution was stable or not for this Reynolds number. Some pioneer works [8,20] and also some more recent works [12,19,23] report stable steady solutions until this value. Definitely, we can assert that the steady solution is not stable any more at $Re = 10{,}000$ as we have proven in the previous section that the first Hopf bifurcation occurs around $Re = 8000$. Some computations on several consecutive grids with various

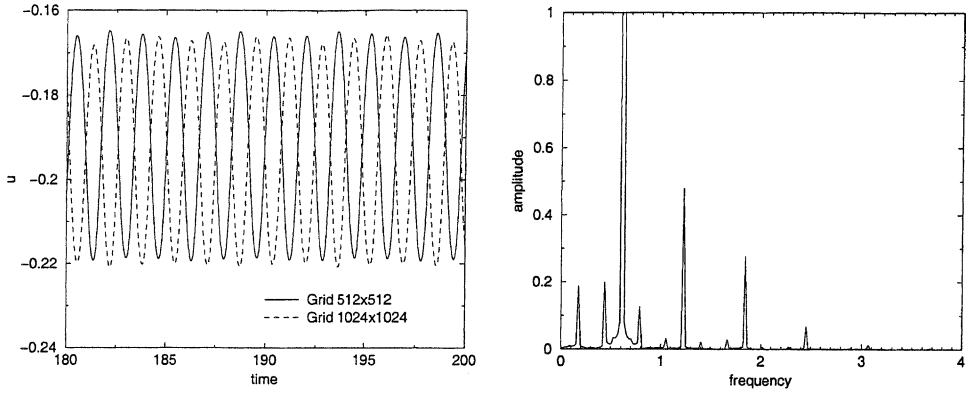

Fig. 7. Horizontal velocity history (left) and power spectrum (right) at monitoring point (14/16,13/16) for $Re = 10{,}000$. Computation with Gear scheme in time and present scheme in space.

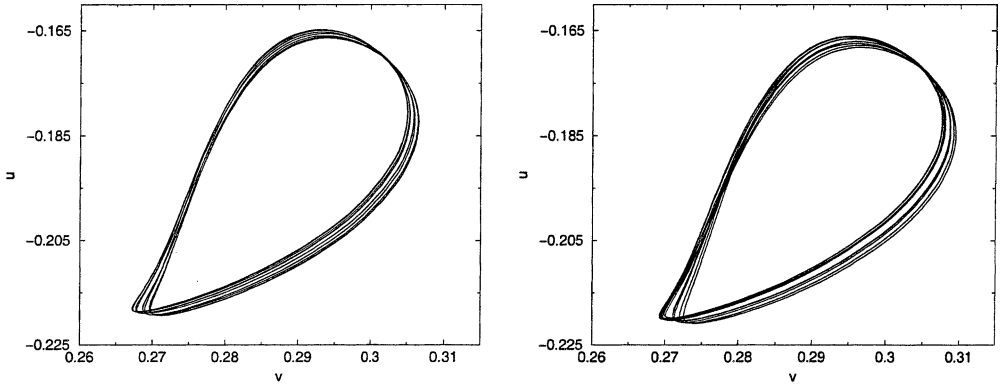

Fig. 8. Phase portrait on grid 512×512 (left) and on grid 1024×1024 (right) at monitoring point (14/16,13/16) for $Re = 10{,}000$. Computation with Gear scheme in time and present scheme in space.

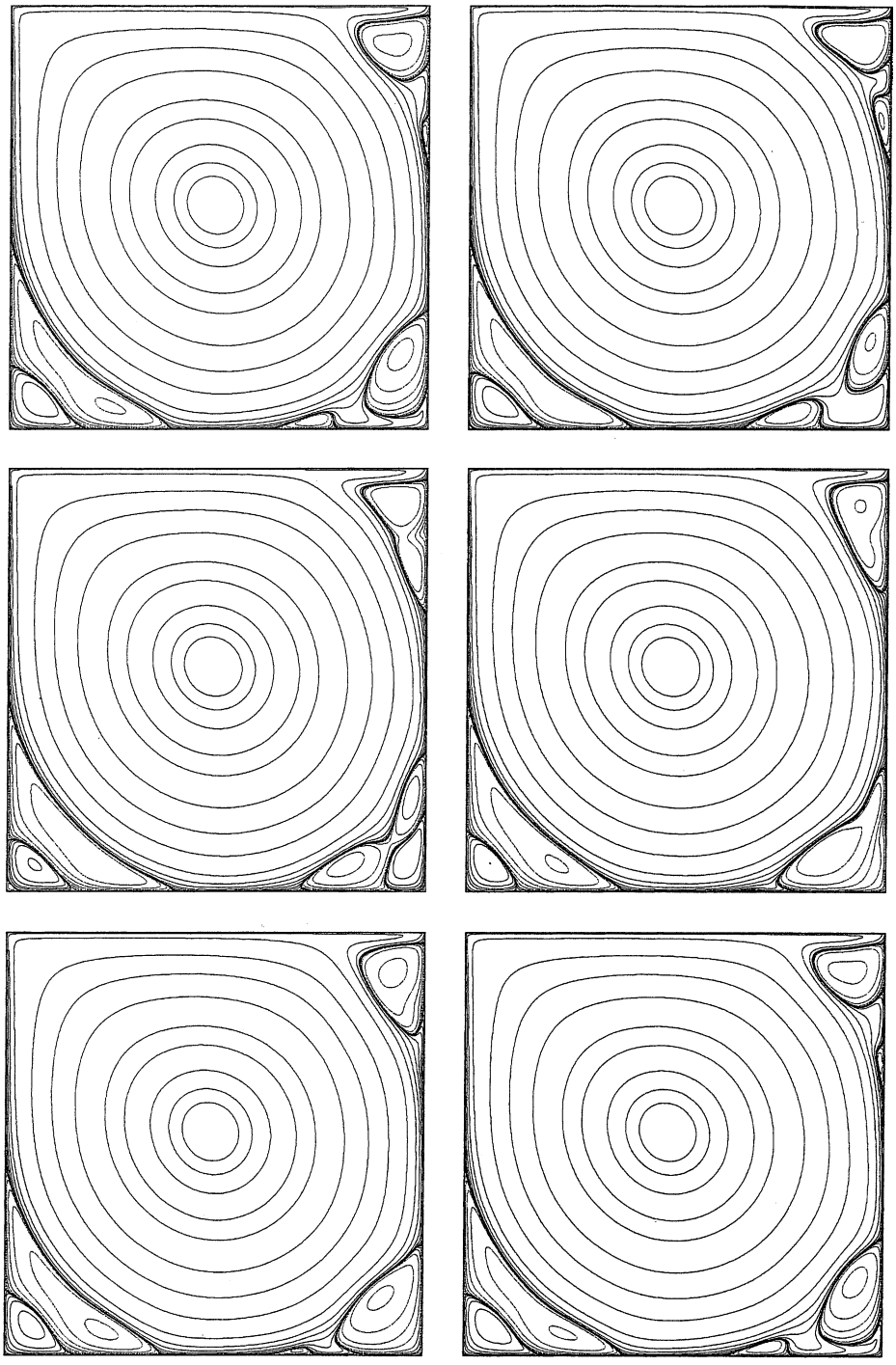

Fig. 9. Evolution of the streamfunction during one main period for $Re = 10{,}000$ on grid 1024×1024. From top to bottom and left to right are represented times $t = 0$, $t = 0.328$, $t = 0.656$, $t = 0.984$, $t = 1.312$ and $t = 1.64$.

initial data show that the stable solution is mainly periodic with small variations in the amplitude of the time evolution at the monitoring points (see Fig. 7). The results on grids 512×512 and 1024×1024 are very similar and give the same main frequency $f = 0.61$. The time history of the kinetic energy is also a periodic signal with the same frequency that oscillates around the mean value $E = 0.046$. The Fourier analysis as well as the phase portraits show that the variations in amplitude yield a solution which is not purely periodic and exhibits some low frequencies $f_2 = 0.175$ and $f_3 = 0.4375$ (Figs. 7 and 8). This shows that we have got a new branch of solutions which is in accordance with the results found in [2] at $Re = 9765$ and in [18] at $Re = 10{,}300$. A computation on a finer 2048×2048 cells grid confirms these results and gives exactly the same frequencies. In Fig. 9 the vorticity field is plotted along a main period from time $t = 0$ to time $t = 1.64$ to show the evolution of the secondary vortices that deform slightly the primary vortex. Indeed, the primary vortex is still attached to the three walls of the cavity but the secondary vortices are unstable. The secondary and tertiary vortices in the bottom left corner are almost stable and pulse slowly whereas the secondary vortices in the two other corners are split into two pieces and reformed along time. The flow patterns of Fig. 9 are very close to those shown in [6].

8. Conclusions

Simulations of the 2D lid-driven cavity flow have been performed for various Reynolds numbers already studied. Highly accurate benchmark results are provided including new global quantities as the kinetic energy and the enstrophy. The results are compared to the best results available in the literature. The first Hopf bifurcation is obtained at Reynolds number close to $Re = 8000$ and a mainly periodic solution is described at $Re = 10{,}000$ with a main frequency $f = 0.61$. The grid convergence is achieved for each Reynolds number but it appears that the numerical simulations on grid 512×512 are accurate enough to well represent the solution even for $Re = 10{,}000$.

References

[1] Aston PJ, Dellnitz M. The computation of Lyapunov exponents via spatial integration with application to blowout bifurcations. Computational methods and bifurcation theory with applications. Comput Methods Appl Mech Eng 1999;170(3–4).
[2] Auteri F, Parolini N, Quartapelle L. Numerical investigation on the stability of singular driven cavity flow. J Comput Phys 2002;183(1).
[3] Botella O, Peyret R. Benchmark spectral results on the lid-driven cavity flow. Comput Fluids 1998;27(4).
[5] Bruneau Ch-H, Jouron C. An efficient scheme for solving steady incompressible Navier–Stokes equations. J Comput Phys 1990;89(2).
[6] Dexun F, Yanwen M, Hong L. Upwind compact schemes and applications, in: Proceedings of the 5th International Symposium CFD, 1993.
[7] Fortin A, Jardak M, Gervais JJ, Pierre R. Localization of Hopf bifurcations in fluid flow problems. Int J Numer Methods Fluids 1997;24(11).
[8] Ghia U, Ghia KN, Shin CT. High-resolutions for incompressible flows using Navier–Stokes equations and a multigrid method. J Comput Phys 1982;48.
[10] Goodrich U. An unsteady time-asymptotic flow in the square driven cavity. In: IMACS 1st International Conference on Computational Physics, Boulder; 1990.

[11] Hackbush W. Multigrid methods and applications. Berlin: Springer-Verlag; 1985.
[12] Huser A, Biringen S. Calculation of two-dimensional shear-driven cavity flows at high Reynolds numbers. Int J Numer Methods Fluids 1992;14(9).
[13] Kawamura T, Takami H, Kuwahara K. New higher-order upwind scheme for incompressible Navier–Stokes equations. Lect Notes Phys 1985;218.
[14] Kim J, Moin P. Application of a fractional-step method to incompressible Navier–Stokes equation. J Comput Phys 1985;59.
[15] Kupperman R. A central-difference scheme for a pure stream function formulation of incompressible viscous flow. SIAM J Sci Comp 2001;23(1).
[16] Leonard BP. The ULTIMATE conservative difference scheme applied to unsteady one-dimensional advection. Comput Methods Appl Mech Eng 1991;88(1).
[17] Pan TW, Glowinski R. A projection/wave-like equation method for the numerical simulation of incompressible viscous fluid flow modeled by the Navier–Stokes equations. Comp Fluid Dyn J 2000;9(2).
[18] Peng Y-F, Shiau Y-H, Hwang RR. Transition in a 2-D lid-driven cavity flow. Comput Fluids 2002;32.
[19] Sahin M, Owens RG. A novel fully-implicit finite volume method applied to the lid-driven cavity problem. Parts I and II. Int J Numer Methods Fluids 2003;42(1).
[20] Schreiber R, Keller HB. Driven cavity flows by efficient numerical techniques. J Comput Phys 1983;49.
[21] Takacs L. A two-step scheme for the advection equation with minimized dissipation and dispersion errors. Mon Weather Rev 1985;113.
[22] Vanka SP. Block-implicit multigrid solution of Navier–Stokes equations in primitive variables. J Comput Phys 1986;65.
[23] Weinan E, Liu J-G. Finite difference schemes for incompressible flows in the velocity-impulse density formulation. J Comput Phys 1997;130(1).